Nonlinear-optical susceptibilities of gases measured at 1064 and 1319 nm

D. P. Shelton
Department of Physics, University of Nevada, Las Vegas, Las Vegas, Nevada 89154
(Received 9 February 1990; revised manuscript received 21 March 1990)

The third-order nonlinear-optical susceptibilities of 16 simple atoms and molecules (Ne, Ar, Kr, Xe, H_2, D_2, N_2, O_2, CO_2, CF_4, SF_6, CH_4, C_2H_6, C_3H_8, n-C_4H_{10}, and C_4H_6) have been measured in the gas phase at two near-infrared wavelengths using the technique of electric-field-induced second-harmonic generation (ESHG) with periodic phase matching and with He as the reference gas. These results are combined with previous ESHG data in the visible region to determine dispersion curves. The experimental estimate of the static hyperpolarizability γ for Ne, $\gamma_{Ne}=119\pm3$ a.u., is in good agreement with the best *ab initio* calculations, but the experimental estimates of the static hyperpolarizabilities for Ar and H_2, $\gamma_{Ar}=1167\pm20$ a.u. and $\langle\gamma^e_{H_2}\rangle=686\pm10$ a.u., differ significantly from the best *ab initio* results.

INTRODUCTION

A wide range of nonlinear-optical processes are mediated by the third-order nonlinear susceptibility $\chi^{(3)}$, which is the macroscopic expression of the microscopic second hyperpolarizability tensor γ.[1-5] There has been much recent interest in third-order nonlinear-optical properties of atoms and molecules, motivated both by the wish to obtain a quantitative understanding of the origin and dynamics of the nonlinear response of atoms and molecules, and by the desire to design better nonlinear-optical materials for applications. For example, organic and polymeric materials are promising candidates for use in nonlinear-optical devices,[6,7] but reliable and accurate calculations of their properties are very difficult, because of their large molecular size, and because of the complex combination of electronic, vibrational, conformational, and orientational contributions to their nonlinear-optical properties. At present, accurate calculations are restricted to much smaller molecules.[8,9]

Productive interplay between theory and experiment requires a common ground for the two, a condition which is met with gas phase nonlinear-optical measurements and *ab initio* calculations for individual small atoms and molecules. *Ab initio* calculations for an isolated molecule determine γ, which is readily compared to the isotropically averaged hyperpolarizability $\langle\gamma\rangle$ measured by nonlinear-optical experiments with a dilute molecular gas. And while small molecules are computationally more tractable, they nevertheless display many of the features also found in larger systems.

An essential complication in the comparison of theory and experiment is the strong frequency dependence of γ. Although now there are an increasing number of dynamic as well as static calculations of γ, many of the most accurate calculations are restricted to the static limit, whereas all experiments measure γ at optical frequencies. The present measurements at near-infrared wavelengths make use of the electric-field-induced second-harmonic generation (ESHG) process, because of the intrinsic accuracy of the technique, and in order that the experimental results may be directly combined with the results of previous ESHG measurements in the visible. In this manner one may determine the dispersion of γ over the widest possible frequency range. One aim is to accurately extrapolate the experimental measurements to the static limit

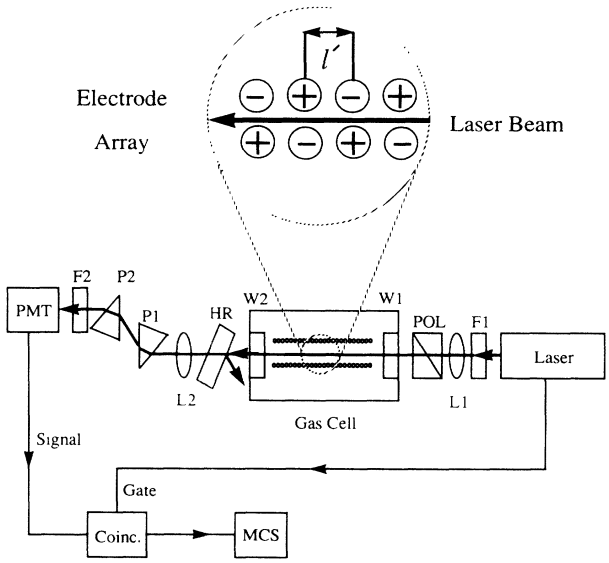

FIG. 1. Schematic diagram of the apparatus. Pulses of about 0.2 mJ, from a Nd:YAG laser, pass through the gas cell. The frequency-doubled beam of light generated in the gas cell is detected by a photomultiplier tube (PMT). Inside the cell, the gas sample through which the laser beam passes is subjected to periodic, transverse electrostatic field of about 1 kV/mm, produced by an array of electrodes with longitudinal repeat distance l'. The optical elements include glass filters (F1,F2), lenses (L1,L2), a polarizer (POL), windows (W1,W2), a high reflector for the fundamental laser beam (HR), and double-Brewster-angle prisms (P1,P2). The apparatus is viewed from above, except for the electrode array which is viewed from the side. The path length from laser to PMT is 3.5 m. The electronics ensure that the output pulses of the PMT are registered only when they are synchronized with the laser pulses.

for direct comparison with the results of *ab initio* calculations. A second aim is to examine the dispersion curves for direct indications of the vibrational contributions expected for molecules. Following a lengthy exposition of the experimental methods, the measurements are presented and analyzed, and the experimental results are considered and compared with the results of *ab initio* calculations.

EXPERIMENTAL METHOD

The experimental method is similar to that previously described,[10–13] but the use of a pulsed near-infrared laser requires revision of many of the details. Accordingly, a relatively complete account of the experimental procedures will be given below. Pulsed operation compensates for a reduction in second-harmonic conversion efficiency when the wavelength is shifted from the visible to the near infrared.

The experiments were performed using a continuously pumped, acousto-optically Q-switched Nd: yttrium aluminum garnet (YAG) laser (CVI model 210 PQT) producing pulses whose wavelength is either $\lambda=1064$ or 1319 nm. The laser beam is weakly focused through a cell containing the sample gas, where second-harmonic generation takes place in the presence of a symmetry-breaking static electric field. A double-prism spectrometer and glass filters serve to separate the second-harmonic from the fundamental laser beam, and a photomultiplier tube (PMT) detects the second-harmonic light. Figure 1 shows the essential optical elements.

The second-harmonic signal generation in the sample is enhanced by means of periodic phase matching. This is accomplished by the use of an array of electrodes which is designed so as to reverse the polarity of the electric field every coherence length $l_c=\pi/\Delta k=\pi/(2k_\omega-k_{2\omega})$, where k_ω is the wave vector at frequency ω in the gas. The resulting periodic phase shift in the generated second-harmonic wave serves to cancel periodically the accumulating phase shift due to normal dispersion, thus allowing the continued growth of the signal throughout the length of the sample. The coherence length of the gas is adjusted to match the fixed spacing of the electrodes by varying the density of the gas until peak signal is achieved.

To calculate the ESHG signal, consider a laser beam propagating through a sample subjected to a transverse electrostatic field varying as $E_0^{(0)}\sin Kz$ within a region of length $2L$ along the beam axis. The power $P^{(2\omega)}$ in the second-harmonic beam, generated from a TEM_{00} Gaussian mode laser beam with confocal parameter z_0 in the sample and beam waist located a distance z_w from the center of the spatially periodic static field region, is given by[10,14]

$$P^{(2\omega)}=\frac{\omega^3(\mu_0/\epsilon_0)^{3/2}}{z_0\pi c n_\omega n_{2\omega}}\left[\chi^{(3)}P^{(\omega)}E_0^{(0)}\int_{-L}^{L}dz\frac{\sin Kz\,\sin[\Delta k\,(z-z_w)-\arctan(z-z_w)/z_0]}{[1+(z-z_w)^2/z_0^2]^{1/2}}\right]^2 . \tag{1}$$

The second-harmonic waves generated at various positions in the sample are described by a Gaussian mode with the confocal parameter z_0', where z_0' differs from z_0 by a small z-dependent correction of order $(n_{2\omega}/n_\omega-1)z_0$ that has been ignored in the derivation. The nonlinear susceptibility $\chi^{(3)}$ mediating ESHG in a low-density gas is given by

$$\chi^{(3)}=\tfrac{1}{4}\mathcal{L}_0\mathcal{L}_\omega^2\mathcal{L}_{2\omega}\langle\gamma\rangle\rho , \tag{2}$$

where $\mathcal{L}_\omega=(n_\omega^2+2)/3$ is the Lorentz local field factor, n_ω is the refractive index at frequency ω, and ρ is the gas density. Since all fields are assumed to be polarized in a common horizontal plane, the spatial subscripts have been omitted from $\chi^{(3)}$ and the isotropically averaged molecular hyperpolarizability tensor $\langle\gamma\rangle$. The wave vector mismatch Δk is negative for normal dispersion and varies as $\lambda^{-3}\rho$, while the refractive index of a low-density gas has only weak linear density dependence.[10,15] An expression for numerically integrating Eq. (1) is given elsewhere.[15] The spatially periodic field is produced by an array of $2N$ electrode pairs with longitudinal spacing l'. When the number of periods of the field $N=KL/\pi$ is large, the integral in Eq. (1) is sharply peaked near $|\Delta k|=K$, with peak height proportional to N^2 and with fractional peak width N^{-1}. Figure 1 shows the configuration of the electrodes. The density dependence of the second-harmonic signal is shown in Fig. 2(a).

In these experiments one determines very accurately the ratio $\chi_A^{(3)}/\chi_B^{(3)}$, by comparing the second-harmonic signals produced under identical phase-matching conditions in sample and reference gases A and B, respectively. Operationally, one varies the gas density and measures the peak second-harmonic signal and the sample density at which this occurs, for each gas in turn. From this information one wishes to extract the ratio of microscopic hyperpolarizabilities $\langle\gamma_A\rangle/\langle\gamma_B\rangle$ for the molecules A and B. The dominant density dependence of $P^{(2\omega)}$ is contained in the factor

$$I^2(\Delta k)=\left[\frac{\Delta k}{K}\int_{-N\pi}^{N\pi}d(Kz)\frac{\sin Kz\,\sin[\Delta k z-\arctan(z/z_0)]}{[1+(z/z_0)^2]^{1/2}}\right]^2 , \tag{3}$$

where, to lowest order in density,

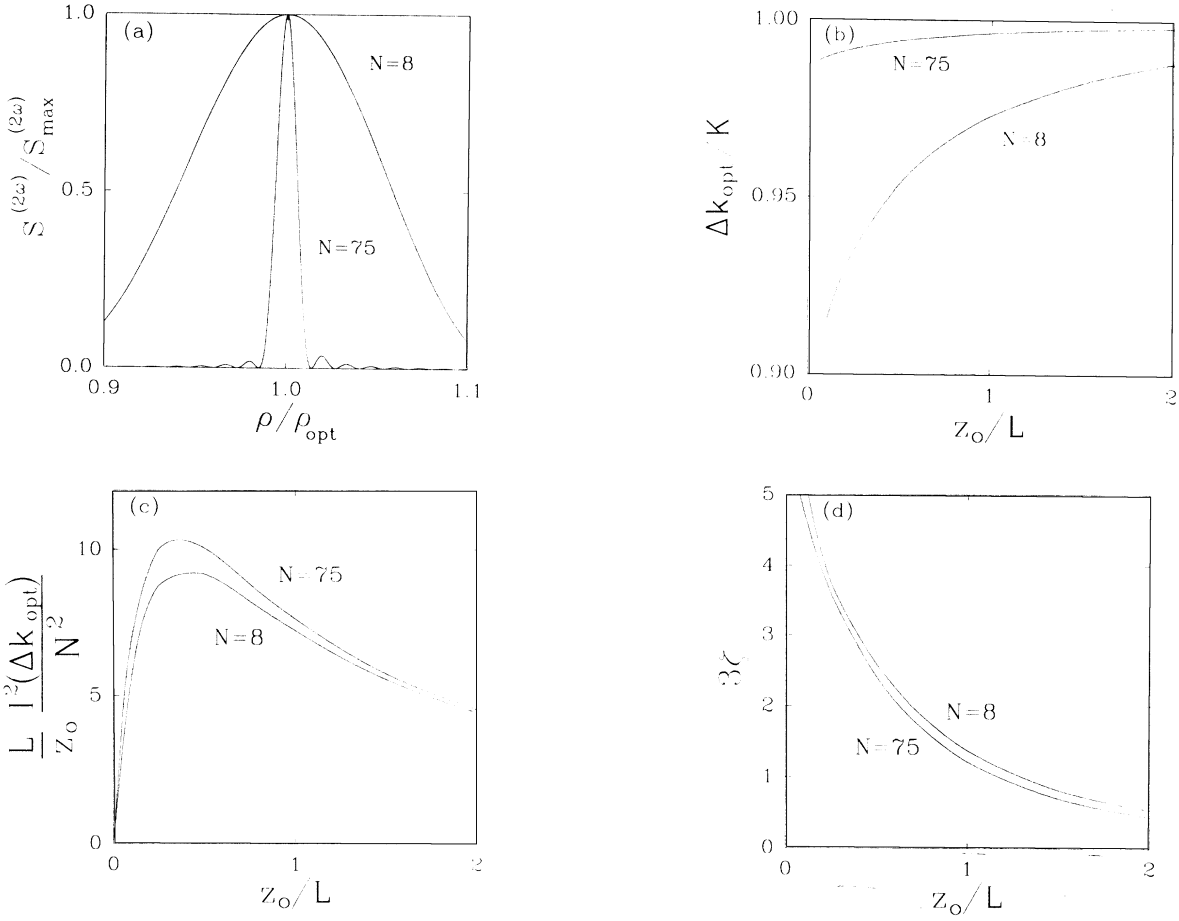

FIG. 2. Calculated results for ESHG with periodic phase matching are compared for two electrode arrays. The coarse electrode array with $N=8$ and $L=20.320$ cm was used for near-infrared ESHG measurements at $\lambda=1319$ nm, while the finer array with $N=75$ and $L=20.193$ cm was used to obtain visible ESHG data. These calculations assume that the laser beam waist is centered in the electrode array ($z_w=0$). (a) The variation of the normalized second-harmonic signal $S^{(2\omega)}$ with normalized sample density ρ is shown for coarse and fine electrode arrays. The confocal parameter $z_0=20$ cm is assumed. Note that the ESHG signal peaks are slightly skew. Less sharply defined phase-matching conditions are obtained with the coarse array, as further illustrated in (b). (b) The gas density at which peak signal occurs, determined by Δk_{opt}, becomes a stronger function of the focusing parameter z_0/L as the number of repeats N of the electrostatic field is reduced. (c) The peak ESHG signal $S^{(2\omega)}$ expressed as photons per second is proportional to $(N^2/L)(\alpha_{2\omega}-\alpha_\omega)^{-2}$ times the function plotted [see Eqs. (1)–(4)], and in the weak focusing limit $z_0/L \gg 1$, $S^{(2\omega)} \propto (\rho_{opt}L/\lambda)^2/z_0$. For $z_0/L \leq 0.5$, obstruction of the fundamental laser beam by the electrodes will be difficult to avoid. Experimentally, the most convenient region is near $z_0/L=1$. In order to keep the phase-match density ρ_{opt} constant for electrode arrays of fixed length L which operate at different wavelengths, one may compensate for the normal λ^3 dependence of ρ_{opt} by scaling N to keep $\lambda^3 N$ constant. Operated at their design wavelengths, the peak ESHG signals from electrode arrays such as the two illustrated here will scale as λ^{-2}. (d) The exponent 3ζ, appearing in Eq. (6), accounts for the small effect on the signal $S^{(2\omega)}$ due to shifts in beam parameters with changing sample refractive index.

$$\Delta k = (-2\pi/\lambda\epsilon_0)(\alpha_{2\omega}-\alpha_\omega)\rho \ , \tag{4}$$

and where the leading factor Δk comes from the factor ρ in Eq. (2) and z_w has been set to zero. The peak of the signal versus density curve identifies essentially identical phase-matching conditions in different gases since $I^2(\Delta k)$ is independent of the particular gas, except through the weak implicit n_ω dependence of z_0 in Eq. (3). The variation, with Δk and z_0, of $I^2(\Delta k)$, the peak position, and peak signal, is shown in Figs. 2(a)–2(c). A more refined estimate of the peak signal must account for the slowly varying refractive index factors, which differ for each gas. The n_ω dependence of $I^2(\Delta k)$ may be made explicit by noting that $z_0=n_\omega z_{00}$, where z_{00} is the fundamental beam confocal parameter in the evacuated sample cell. Expanding Eq. (3) as a Taylor series in $(n_\omega-1)$ and using $1+\zeta(n_\omega-1)\approx n_\omega^\zeta$, one may approximate the peak value

I_m^2 of $I^2(\Delta k)$ as $I_m^2 \approx n_\omega^\zeta I^2_{m,n_\omega=1}$, where $\zeta=(I_m^{-2}dI_m^2/dn_\omega)_{n_\omega=1}$. Treating Eqs. (1) and (2) in a similar fashion, one may express all the explicit and implicit dependence of $P^{(2\omega)}$ on n_0, n_ω, and $n_{2\omega}$ in the form of a factor $n_0^\alpha n_\omega^\beta n_{2\omega}^\gamma$. This factor slightly changes the peak value of Eq. (1) but has a negligible effect on the value of Δk at which the peak occurs. Higher Fourier components of the periodic electrostatic field have a small effect on the ESHG signal peak, but this is independent of the particular gas sample and so may be ignored. Equations (1) and (2) may be solved for $\langle\gamma\rangle$, and if the laser beam parameters are kept fixed, one obtains

$$\frac{\langle\gamma_A\rangle}{\langle\gamma_B\rangle}=\left[\frac{S_A^{(2\omega)}}{S_B^{(2\omega)}}\right]^{1/2}\left[\frac{n'_A\rho_A V_A}{n'_B\rho_B V_B}\right]^{-1}, \tag{5}$$

where $S^{(2\omega)}$ and ρ are the maximum ESHG signal and the optimum sample density, V is the voltage applied to the electrodes, and

$$n'=(n_0^4 n_\omega^{2+3\zeta} n_{2\omega})^{1/6}. \tag{6}$$

The value of 3ζ is plotted in Fig. 2(d) as a function of the focusing parameter z_0/L and the number of periods N of the static field. One finds that $3\zeta\approx 1$ when the focusing parameter falls in the experimentally convenient range $1\le z_0/L\le 1.5$. Figure 2(c) shows that for this range of z_0/L values the ESHG signal is about $\frac{2}{3}$ of its maximum possible value. The analysis of the experimental results makes use of Eqs. (5) and (6) with $3\zeta=1$.

Next we return to a more detailed consideration of the experimental design and operating parameters. Referring back to Fig. 1, one sees that the presample optics include an infrared-transmitting filter (RG-850) which blocks any second-harmonic light and most of the stray pump light from the laser, a lens which focuses the laser beam at the center of the sample cell with a confocal parameter of $z_0=20$ cm, and a Glan-laser prism polarizer to select the desired polarization state of the beam. The average power of the unpolarized, TEM_{00} laser output beam is about 1.3 W when operating at $\lambda=1064$ nm with a Q-switch repetition rate of 5000 Hz. The laser pulses have a duration of 150 ns full width at half maximum (FWHM), and the width of the laser output pulse height distribution is 16% FWHM. The polarized beam inside the sample cell has an average power of about 0.45 W and a peak power of about 500 W. For $\lambda=1319$ nm operation, the laser is Q switched at 2500 Hz and the average and peak powers are reduced to about 70% of those for $\lambda=1064$ nm operation. The laser has the unfortunate tendency, when operating at $\lambda=1319$ nm, of simultaneously operating on the $\lambda=1338$ nm laser line with up to 10% of the output power appearing in the second laser line.[16] When this occurs, the experimental measurements become very erratic and are discarded. Another source of erratic results at both laser wavelengths is temperature cycling of the laser-head cooling water; the laser was modified to stabilize the water temperature to better than 0.1 °C in order to eliminate this problem.

The output beam from the sample cell passes through a dichroic mirror which reflects >99.5% of the fundamental laser beam, a collimating lens, a pair of fused-silica double-Brewster-angle dispersing prisms, and an infrared-blocking filter (KG-3), finally reaching the detector. For experiments at $\lambda=1064$ nm the detector is an uncooled EMI 9893 QB/350 PMT with a bialkali photocathode, operating in photon counting mode. This PMT has a quantum efficiency of about 10% at $\lambda=532$ nm but is blind to light from the laser that passes through the combined Schott RG-850 and KG-3 filters, resulting in a background count rate of 1 count per second (counts/s). For experiments with the laser operating at $\lambda=1319$ nm, the second-harmonic light at $\lambda=660$ nm is detected by a cooled RCA 31034 PMT with a GaAs(Cs) photocathode having high quantum efficiency in the red. Since this PMT is sensitive to the light near $\lambda=850$ nm which leaks through the combined glass filters, the background count rate in this case is much higher, near 40 counts/s.

The electrode array is constructed from two parallel steel bars, each of which has two rows of holes drilled and reamed to accept the 3.175-mm-diam polished steel dowel pins which serve as the actual electrodes. The longitudinal and transverse spacing between the centers of the holes is 5.080 mm. The longitudinal spacing of the electrode pairs l' may be selected as a multiple of the spacing between the holes by choosing the holes into which the pins are inserted. The length of the electrode array is up to 41 cm. Other than using drilled holes to hold the electrodes and having a coarser electrode spacing, the construction of the electrode array is similar to that previously described.[12] A longitudinal spacing $l'=15.240$ mm, with $2N=28$ electrode pairs, was selected for the measurements at $\lambda=1064$ nm. For $\lambda=1319$ nm the spacing was increased to $l'=25.400$ mm and the number of electrode pairs was reduced to $2N=16$, approximately compensating for the λ^3 dependence of the coherence length of the gas at constant density.[15] Typical operating conditions at $\lambda=1064$ nm, with N_2 sample gas, were $p=4.3$ atm, $V=2000$ V, and $S^{(2\omega)}=800$ counts/s. Phase-match pressure varied from 90 atm for He to only 0.3 atm for butadiene, while V was in the range 0.8–3.6 kV (well below the breakdown voltage). At $\lambda=1319$ nm, p and V were about 15% and 50% larger, and $S^{(2\omega)}$ was reduced to about 400 counts/s.

Dead time in the photon counting electronics could not be ignored, even though the average count rate of the detector was less than 10^3 counts/s, because the second-harmonic photons are generated only during the 150-ns-wide laser pulses. The configuration of the electronics was chosen with this in mind. The PMT output pulses are used to trigger 1-μs-duration logic pulses; these pulses are sent to one input of a coincidence module which has a 1-μs coincidence resolving time. Logic pulses of 1 μs duration and synchronized with the laser output pulses are generated and sent to the second input of the coincidence module. Output logic pulses from the coincidence module are registered by a multichannel scalar (MCS). This arrangement serves two purposes. First, it reduces the effective background count rate by a large factor, since PMT pulses cannot be registered unless they fall within a 1-μs time window centered on each laser output pulse. Thus, the effective background is reduced

to 0.01 counts/s for $\lambda=1064$ nm and to 0.1 counts/s for $\lambda=1319$ nm (in each case about 0.005 counts/s of the total is due to coherent second-harmonic background). Second, this arrangement of the electronics makes the dead time corrections accurately calculable. Let $\bar{n}$ be the average number of PMT output pulses produced per laser pulse. Assuming Poisson statistics, the probability that there will be at least on PMT output pulse per laser pulse is $P(\bar{n})=1-\exp(-\bar{n})$. Because the coincidence resolving time of 1 μs is much longer than the time during which essentially all second-harmonic photons are produced for each laser pulse (0.1 μs), the measured signal count rate S is just $S=RP$, where R is the laser pulse repetition rate. The true count rate $\tilde{S}=R\bar{n}$ (i.e., the rate that would be measured with zero dead time) is given by

$$\tilde{S}=-R\ln(1-S/R)\ . \tag{7}$$

This relation was tested by determining $\tilde{S}/V^2$ versus V^2 with our apparatus, where $\tilde{S}/V^2$ should be independent of V^2 if $\tilde{S}$ is correctly calculated. Choosing experimental parameters such that $10^{-2}\le\bar{n}\le 1$, the relation $\tilde{S}/V^2=$const was confirmed at the 0.5% level of accuracy (note that the counting efficiency has fallen to 63% for $\bar{n}=1$).

In order to make the experimental results insensitive to small inaccuracies of the dead time corrections, sample and reference signals were arranged to be nearly equal by appropriate adjustments of the electrode array voltage. The approximate result $\tilde{S}_A/\tilde{S}_B\approx[1-(S_A-S_B)/2R](S_A/S_B)$ shows that the dead time correction to the ratio S_A/S_B is only 0.5% when $S_A/R=0.1$ and $S_A/S_B=1.1$. Furthermore, matching the signal strengths also reduces the systematic error in the ratio S_A/S_B due to the presence of a coherent second-harmonic background b, where $S_A/S_B\rightarrow(1+\epsilon)S_A/S_B$ and $\epsilon=\pm(b/S_B)^{1/2}(S_A-S_B)/S_B$ in the presence of the coherent background. For the ESHG measurements reported here, the signals S_A and S_B were matched to about 1% and $\bar{n}=\tilde{S}/R$ was in the range 0.04–0.16.

Two other possible sources of systematic errors are misalignment of the static and optical field polarizations, and stress birefringence of the cell windows. Misalignment of the static field will cause systematic errors in the ratio S_A/S_B which vary as θ^2, but only if there is a difference in the deviations from Kleinman symmetry for A and B.[11] If the deviations from Kleinman symmetry are no larger than 10%, then a misalignment of $\theta=5°$ will result in a systematic error no larger than 0.01%. The actual misorientation was only about 0.5°. A more serious concern was the stress birefringence of the entrance window, which reduces the ESHG signal in this apparatus by the factor $(1-2.4\Delta_1^2)$, where $\Delta=\frac{1}{2}\delta\sin2\phi$, δ is the retardation, and ϕ is the angle between the strain axis of the window and the optical polarization. Because of the polarization selectivity of the prism spectrometer, birefringence of the exit window of the sample cell also reduced the ESHG signal, but the sensitivity to the second window was five times smaller. Systematic errors in S_A/S_B arise because the window stress birefringence varies with gas pressure, and so it is not the same for both gases A and B. Care was taken to reduce the stress birefringence of the fused-silica gas cell windows by supporting them on symmetrical, optically flat steel mounts at normal incidence to the beam. The effect of the typical $\delta=10$ mrad retardation of a nominally unstressed window was minimized by carefully orienting the stress axis along the laser beam polarization direction. The window stress birefringence was assessed by placing a crossed polarizer after the sample cell and measuring the extinction ratio $r=(\Delta_1+\Delta_2)^2$, employing a $\lambda=514.5$ nm laser beam, while varying the gas pressure in the range 0–150 atm. The extinction ratio varied as p^2, reaching $r\approx2\times10^{-4}$ at the He phase-match pressure. Accounting for the λ^{-1} dependence of the retardation δ, one may infer that the maximum systematic error in the ratio S_A/S_B due to window stress birefringence was only 0.01%. In summary, adjustments to the apparatus made systematic corrections to the ESHG measurements negligible, except for the dead time correction to the signal given by Eq. (7).

Measurements were made in coupled triplets ($ABABA\cdots$) in order to cancel drifts. The ESHG peak for each gas was scanned twice before interchanging sample and reference gases in the cell. Signal counts were accumulated for 20 s in each MCS channel, while the pressure was scanned at a rate of 0.1–0.2 % per channel, and synchronized pressure (and temperature) readings were recorded. The peak signal and phase-match pressure were determined from a quadratic least-squares fit to the ESHG signal data, using only data within 15% of peak signal to avoid fitting errors and to minimize the effect of pressure scan nonlinearity. Statistical uncertainty for a single peak intensity determination was typically 0.1–0.2 %. The hyperpolarizability ratios were obtained from the raw measurements by first correcting the measured peak signals with Eq. (7), and then using Eqs. (5) and (6) with $3\zeta=1$. Sample densities were computed from the measured pressures and temperatures using the virial equation of state.[17] The typical virial correction was $<1\%$, while the largest correction was about 5% for He. The random uncertainty is 0.1% for a single phase-match-density determination. Pressures were measured with either a Bourdon-tube gauge accurate to 0.1% of full scale (160 bars), or at pressures below 10^4 Torr, with a capacitance manometer with a relative accuracy of 0.15%. Temperature was measured to 0.1 °C with a calibrated thermistor thermometer in contact with the sample gas. All measurements were made at room temperature (21–23 °C). The measurement temperature was 22.0 ± 0.2 °C for the gases C_3H_8, n-C_4H_{10}, and C_4H_6, for which the effective $\langle\gamma\rangle$ may have temperature dependence due to a $\mu^{(0)}\beta/3kT$ term. Refractive indices were calculated from tables using the measured densities,[18,19] with the resulting values of $n'-1$ in the range $(1-4)\times10^{-3}$. The electrode voltage was measured by means of a voltage divider and voltmeter with an overall accuracy of 0.01%. High-purity gases were employed. The minimum purity was 99.999% for He, Ne, Ar, H_2, D_2, and N_2; 99.995% for Kr and Xe; 99.99% for CO_2, SF_6, C_2H_6, and C_3H_8; 99.97% for CH_4; 99.9% for CF_4; 99.6% for O_2; 99.5% for butadiene; and 99.0% for

n-C_4H_{10}. Analysis of the butane on a gas-chromatograph mass spectrometer indicates that the actual impurities were 0.3% neopentane and 0.02% isobutane, which may be expected to shift $\langle\gamma\rangle$ for the sample by less than 0.1% compared to pure n-butane.[20,21] Except for the cases of butadiene and O_2, where sample impurities may possibly introduce systematic errors $>0.1\%$, the experimental uncertainty of the hyperpolarizability ratio determinations is just the convolution of the statistical uncertainty for an average of three triplets of measurements and the uncertainty of the density determinations due to the limited pressure gauge accuracy. The uncertainty of the ratio $\langle\gamma_A/\gamma_B\rangle$ is about $\pm0.4\%$ (range $\pm0.1-\pm0.7\%$).

DATA ANALYSIS

The ratios of phase-match densities and hyperpolarizabilities determined for 16 atoms and molecules in these ESHG experiments are presented in Table I. Inspecting the values of $\langle\gamma_A\rangle/\langle\gamma_B\rangle$ obtained at $\lambda=1319$ nm and at $\lambda=1064$ nm for each choice of A and B, one finds only small, though significant, differences in the values at the two wavelengths. This is as one would expect, and tends to support the accuracy of the experimental results, but also demonstrates that a more refined analysis is needed to extract information about the contributions to γ due to electronic, vibrational, and other degrees of freedom of the molecules. The phase-match density ratios, $\rho_B/\rho_A\approx(\alpha_{2\omega}-\alpha_\omega)_A/(\alpha_{2\omega}-\alpha_\omega)_B$, are more sensitive in this regard. For atoms and homonuclear diatomic molecules there is no vibrational contribution to α_ω, and since ω is far below electronic resonance, $(\alpha_{2\omega}-\alpha_\omega)$ should increase steadily with increasing ω. But for the polyatomic molecules, the vibrational resonances at infrared frequencies should also increase the dispersion of α at low-enough frequencies, making $(\alpha_{2\omega}-\alpha_\omega)$ decrease with increasing ω for near-infrared wavelengths. Consideration of the frequency dependence of the results for ρ_B/ρ_A immediately allows one to divide the molecules into three classes: ρ_B/ρ_A for the atoms and homonuclear diatomic molecules increases by $\leq1\%$ going from $\lambda=1319$ nm to $\lambda=1064$ nm, reflecting the purely electronic contributions to α_ω; ρ_B/ρ_A for the molecules CO_2, CF_4, and SF_6 decreases sharply, by 40%, reflecting a strong vibrational contribution to α_ω; and ρ_B/ρ_A for the alkanes decreases only slightly, by 4%, reflecting relatively minor vibrational contributions to α_ω. More quantitative analysis bears out this categorization.[22,23]

The first step in the analysis of the hyperpolarizability data is extraction of $\langle\gamma\rangle$ from the measured ratios. This is done in several stages. Since the ultimate reference for all the measurements is the theoretical result for γ_{He}, the data calibrated directly with He are treated first, and they in turn serve as secondary reference standards in the reduction of the remaining data.

The best available *ab initio* calculation for γ_{He} is that of Bishop and Pipin,[24] which uses explicitly electron-correlated wave functions to evaluate a sum-over-states expression for γ; each of the ^1S, ^1P, and ^1D states of He is expressed as a sum of up to 140 basis functions which can represent ss', sp, sd, and pp configurations. Dynamic hyperpolarizabilities are calculated for the dc Kerr effect,

TABLE I. Experimental results for the ratios of phase-match densities, ρ_B/ρ_A, and ratios of hyperpolarizabilities, $\langle\gamma_A\rangle/\langle\gamma_B\rangle$, measured at $\lambda=1319$ nm and $\lambda=1064$ nm. A and B denote the sample and reference gases, respectively, for a given ESHG measurement. The measurements of γ_{Ar}/γ_{He}, $\langle\gamma_{N_2}\rangle/\gamma_{He}$, and $\gamma_{Ar}/\langle\gamma_{N_2}\rangle$ form an overdetermined set; the values given in the table have been adjusted to maximize the self-consistency of this set. The density ratios ρ_{H_2}/ρ_{D_2} and ρ_{N_2}/ρ_{Ar} are so close to 1 that the differential linearity rather than the absolute accuracy of the capacitance manometer determines the gauge calibration uncertainty; the stated uncertainty for these measurements is essentially the statistical uncertainty.

		ρ_B/ρ_A		$\langle\gamma_A\rangle/\langle\gamma_B\rangle$	
A	B	$\lambda=1319$ nm	$\lambda=1064$ nm	$\lambda=1319$ nm	$\lambda=1064$ nm
Ne	He	1.853±0.004	1.850±0.007	2.534±0.019	2.487±0.011
Ar	He	18.41±0.03	18.54±0.05	27.84±0.16	27.98±0.08
Kr	Ar	2.019±0.004	2.031±0.004	2.244±0.005	2.296±0.006
Xe	Ar	4.686±0.010	4.727±0.009	6.025±0.013	6.136±0.015
H_2	He	13.16±0.03	13.28±0.03	15.10±0.05	15.77±0.04
D_2	H_2	0.9720±0.0005	0.9717±0.0002	1.013±0.003	1.002±0.001
N_2	He	19.83±0.05	19.93±0.05	21.75±0.13	21.82±0.07
O_2	N_2	1.185±0.003	1.200±0.003	1.054±0.005	1.067±0.003
Ar	N_2	0.9282±0.0002	0.9295±0.0005	1.280±0.004	1.282±0.002
CO_2	N_2	2.530±0.008	2.031±0.004	1.263±0.008	1.283±0.008
CF_4	N_2	2.345±0.005	1.558±0.003	1.082±0.007	1.084±0.005
SF_6	N_2	3.144±0.007	2.321±0.005	1.542±0.008	1.530±0.008
CH_4	N_2	2.240±0.005	2.166±0.005	2.757±0.012	2.931±0.010
C_2H_6	N_2	3.899±0.009	3.742±0.009	5.39±0.03	5.53±0.03
C_3H_8	N_2	5.662±0.015	5.440±0.015	9.03±0.03	9.14±0.03
n-C_4H_{10}	N_2	7.35±0.02	7.07±0.02	11.54±0.05	11.69±0.04
C_4H_6	N_2		14.61±0.08		20.88±0.11

TABLE II. Coefficients of the truncated power series $\gamma=\gamma_0(1+A\nu_L^2+B\nu_L^4+C\nu_L^6)$, fit to the *ab initio* values of γ_{He} for ESHG (where $\nu_L^2=6\nu^2$ and ν is given in units of cm^{-1}) (Ref. 24). The coefficients in the column headed "atomic units" pertain to the expansion in terms of ω_L^2 (a.u.).

	Atomic units	SI units
γ_0	43.104	2.6903×10^{-63} $C^4m^4J^{-3}$
A	2.191	4.550×10^{-11} cm^2
B	3.381	1.458×10^{-21} cm^4
C	6.748	6.043×10^{-31} cm^6

degenerate four-wave-mixing (DFWM), ESHG, and third-harmonic generation (THG) nonlinear-optical processes, for frequencies up to $\omega=0.20$ a.u. The estimated convergence error of about 0.02% is also the estimated accuracy of these results.[24,25] To make use of the results of this calculation to calibrate our experimental data, we have fitted a dispersion curve to the calculated γ_{He} values. The frequency dependence of γ_{He} for each nonlinear-optical process may be represented at low frequencies by truncating the power-series expansion

$$\gamma(-\omega_\sigma;\omega_1,\omega_2,\omega_3)=\gamma_0(1+A\omega_L^2+B\omega_L^4+C\omega_L^6+\cdots), \tag{8}$$

where $\gamma_0=\gamma(0;0,0,0)$, $\omega_\sigma=\omega_1+\omega_2+\omega_3$, and $\omega_L^2=\omega_\sigma^2+\omega_1^2+\omega_2^2+\omega_3^2$. For ESHG one has $\gamma(-2\omega;0,\omega,\omega)$ and $\omega_L^2=6\omega^2$. A rigorous calculation has shown that the first dispersion coefficient A in this power-series expansion of γ is exactly the same for all nonlinear processes in a given atom.[26] The coefficients in Eq. (8) were determined for He by making a least-squares fit of the function $A+B\omega_L^2+C\omega_L^4$ to the values of $(\gamma/\gamma_0-1)/\omega_L^2$ versus ω_L^2, over the interval $0.004\le\omega_L^2\le0.08$ a.u. (where roundoff errors and the contributions of higher terms were both small). The fit included data for all four nonlinear-optical processes: the coefficients B and C were allowed to differ for each pro-

TABLE III. Experimental values of $\langle\gamma\rangle_{zzzz}$ from gas phase ESHG measurements at 34 near-infrared and visible wavelengths. The values at $\lambda=1319$ nm and 1064 nm are from the present work, while the values at the other wavelengths are from the literature. The stated uncertainties for $\langle\gamma\rangle$ do not include an allowance for the calibration uncertainty (see text). Wavelengths λ are those measured in air, while wavenumbers ν are those measured in vacuum. (a) Measurements of $\langle\gamma\rangle$ for Ar, H_2, and N_2 made directly against He, which is the ultimate reference for all the measurements. The tabulated values of $\langle\gamma^{vR}\rangle$ for H_2 and D_2 at $T=295$ K were calculated as discussed in the text. The values of $\langle\gamma\rangle$ for D_2 and O_2 were calibrated using the smooth fitted curves for $\langle\gamma_{H_2}\rangle$ and $\langle\gamma_{N_2}\rangle$, respectively. (b) Measurements of γ_{Ne}, calibrated directly against γ_{He}; measurements of γ_{Kr} and γ_{Xe}, calibrated using the smooth fitted curve for γ_{Ar}; and measurements of $\langle\gamma\rangle$ for SF_6, C_2H_6, C_3H_8, and n-C_4H_{10}, calibrated using the smooth fitted curve for $\langle\gamma_{N_2}\rangle$. (c) Measurements of $\langle\gamma\rangle$ for CH_4, CF_4, CO_2, and C_4H_6, calibrated using the smooth fitted curve for $\langle\gamma_{N_2}\rangle$.

		(a) $\langle\gamma\rangle$ (10^{-63} $C^4m^4J^{-3}$)						
λ (nm)	ν (cm^{-1})	Ar (Ref. 28)	H_2 (Ref. 13)	H_2^{vR}	D_2 (Ref. 13)	D_2^{vR}	N_2 (Ref. 28)	O_2 (Ref. 28)
1319[a]	7 581	76.09±0.43	41.27±0.13	−3.52	41.70±0.12	−1.61	59.44±0.36	62.06±0.29
1064[a]	9 395	77.12±0.22	43.47±0.10	−2.25	43.63±0.05	−0.99	60.14±0.19	64.31±0.18
700.0	14 282	84.45±0.71	49.90±0.31	−0.84			65.58±0.43	71.93±0.85
694.3	14 399	84.30±0.77	49.97±0.28	−0.83	48.73±0.17	−0.40	66.01±0.40	72.71±0.80
690.0	14 489	84.85±0.71	50.21±0.23	−0.82			65.60±0.34	72.36±0.80
680.0	14 702	85.77±0.48	50.18±0.26	−0.79			65.92±0.34	73.26±0.77
670.0	14 921	84.58±0.74	50.79±0.26	−0.77			66.27±0.34	74.13±0.63
660.0	15 147	85.83±0.80	50.65±0.20	−0.74	49.86±0.14	−0.36	66.62±0.32	74.65±0.60
650.0	15 380	87.32±0.52	51.39±0.23	−0.72			67.50±0.32	75.57±0.66
640.0	15 620	86.90±0.40	51.35±0.17	−0.69			67.99±0.26	75.70±0.66
632.8	15 798	87.09±0.49	51.55±0.23	−0.68	50.84±0.14	−0.33	68.38±0.29	75.79±0.58
620.0	16 124	88.91±0.61	52.59±0.23	−0.65			68.70±0.38	77.14±0.61
610.0	16 389	89.50±0.58	53.10±0.26	−0.63	51.54±0.19	−0.30	68.61±0.32	77.50±0.64
600.0	16 662	90.05±0.46	53.38±0.26	−0.61			69.71±0.26	78.28±0.64
590.0	16 944	91.05±0.47	54.25±0.20	−0.58	52.42±0.15	−0.28	70.66±0.26	79.34±0.67
580.0	17 236	91.40±0.56	54.81±0.23	−0.56			71.00±0.26	80.56±0.76
514.5	19 430	97.22±0.51	59.22±0.24	−0.44	57.14±0.17	−0.21	75.46±0.33	89.48±0.78
496.5	20 135	100.23±0.96	60.45±0.39	−0.41	58.65±0.19	−0.20	76.76±0.39	93.30±1.05
488.0	20 487	101.37±0.67	61.13±0.30	−0.39	59.65±0.19	−0.19	78.25±0.39	94.29±0.94
476.5	20 981	104.50±0.67	62.55±0.46	−0.37	60.85±0.30	−0.18	79.75±0.61	96.89±1.46
457.9	21 831	105.85±1.42	64.82±0.77	−0.34			82.90±0.89	

TABLE III. (*Continued*).

(b)

λ (nm)	ν (cm^{-1})	$\langle\gamma\rangle$ (10^{-63} $C^4m^4J^{-3}$) Ne (Ref. 30)	Kr (Ref. 29)	Xe (Ref. 29)	SF_6 (Ref. 31)	C_2H_6 (Ref. 33)	C_3H_8 (Ref. 33)	n-C_4H_{10} (Ref. 33)
1319[a]	7 581	6.925±0.051	169.7±0.4	455.5±1.0	90.8±0.5	317±2	532±2	680±3
1064[a]	9 395	6.855±0.030	177.4±0.5	474.1±1.2	92.2±0.5	333±2	551±2	705±2
670.0	14 921				98.2±0.5			
650.0	15 380		204.6±0.5	586.5±2.3	99.2±0.5			
620.0	16 124				99.9±0.8			
616.1	16 227					431±2	746±6	969±15
594.4	16 817	6.402±0.087						
590.0	16 944		217.4±1.0	645.1±1.9				
514.5	19 430	6.816±0.060	242.5±0.7	754.3±2.8	109.1±0.2	503±3	890±6	1176±13
488.0	20 487	7.141±0.091	254.4±0.7	809.1±3.1	112.0±0.4	546±5	958±7	1278±14
457.9	21 831				115.2±3.0			

(c)

λ (nm)	ν (cm^{-1})	$\langle\gamma\rangle$ (10^{-63} $C^4m^4J^{-3}$) CH_4 (Ref. 32)	CF_4 (Ref. 23)	CO_2 (Ref. 22)	C_4H_6 (Ref. 34)
1319[a]	7 581	162.33±0.71	63.71±0.41	74.37±0.47	
1064[a]	9 395	176.65±0.60	65.33±0.30	77.33±0.48	1258±7
694.3	14 399				1708±97
692.9	14 427			85.27±0.33	
671.7	14 883	206.76±0.47			
671.5	14 888	206.46±0.60			
667.8	14 970	207.06±0.47			
659.8	15 152		71.83±0.27		
650.7	15 369	211.07±0.54		87.62±0.27	
640.2	15 615		72.31±0.27		
621.7	16 080		73.22±0.27		
619.0	16 151	217.65±0.55			
616.1	16 227	217.99±0.55		90.00±0.34	
589.0	16 973	225.27±0.56	74.41±0.14		
514.5	19 430	253.16±1.44	79.05±0.23	100.58±0.23	
501.7	19 926	260.23±0.77			
496.5	20 135	263.02±0.93	80.14±0.31		
488.0	20 487	268.29±0.78	81.13±0.23	105.01±0.39	
476.5	20 981	275.25±1.51			

[a] Present work.

cess, but the coefficient A was constrained to be identical for all four. The coefficient $A=2.191$ a.u. obtained in this way is a good estimate (±0.001 a.u.) of the coefficient A in the infinite power series expansion, though the coefficients B and C are not. The fit coefficients obtained for the ESHG process in He are given in Table II. This fit represents the *ab initio* results for He to better than 0.01% for $\omega_L^2 \leq 0.08$ a.u. ($\lambda \geq 395$ nm). Finally, before being used for calibration, the γ_{He} results must be converted from atomic units to SI units. Accounting for the effect of the finite ^{4}He nuclear mass by means of scaling factors [$\omega=\omega_\infty(\mu/m_e)$ and $\gamma=\gamma_\infty(\mu/m_e)^{-7}$] involving the reduced electron mass μ, and using the 1986 CODATA values of the fundamental constants,[27] the conversion factors for the He atom are: ω, 1 a.u.=219 444.5464 cm^{-1}; and γ, 1 a.u.=6.241 363×10^{-65} $C^4m^4J^{-3}$. The fit coefficients for γ_{He} expressed in SI units are also given in Table II.

In addition to the data given in Table I, there are also previous ESHG hyperpolarizability ratio measurements of comparably high accuracy, made at visible laser wavelengths. Combining the near-infrared and visible data allows one to accurately describe the frequency dependence of γ and to make a meaningful extrapolation to the static limit of γ. The visible ESHG data to be included in our analysis is given in Ref. 13 (H_2, D_2), Ref. 22 (CO_2), Ref. 23 (CF_4), Ref. 28 (Ar,N_2,O_2), Ref. 29 (Kr,Xe), Ref. 30 (Ne), Ref. 31 (SF_6), Ref. 32 (CH_4), Ref. 33, (C_2H_6,C_3H_8,n-C_4H_{10}), and Ref. 34 (C_4H_6). Ward and co-workers have also made ESHG measurements at $\lambda=694.3$ nm, with stated accuracy of 1–2 %, for a number of molecules in the present study.[35] These and other

relevant nonlinear-optical measurements had been considered previously and found to be consistent with the data in our chosen sample. Since these other data are of uneven quality and would have at most a marginal effect on our fits, they are not considered here.

The experimental estimates of γ_{Ar} and γ_{Ne}, computed from the measured ratios using the fitted values for γ_{He}, are given in Tables III(a) and III(b). Just as for He, we wish to obtain dispersion curves which represent the data. For the atoms Ne and Ar it is sufficient to use a truncated power series in ν_L^2, with the form given by Eq. (8), and with coefficients γ_0, A, and B determined by a weighted least-squares fit to the data. The fit coefficients are given in Table IV, and the data and the fitted curves are shown in Figs. 3(a) and 3(b). The negative dispersion at low frequencies seen in the case of Ne is anomalous, as has already been noted and discussed.[30] While surprising, such behavior for γ is allowed by the quantum-mechanical expression for γ, and it also resolves the apparent discrepancies between the results of various experimental measurements and *ab initio* calculations of γ for Ne. This unusual behavior seems to be due to strong electron-correlation effects for γ_{Ne}, and merits further study. The smooth, monotonic dispersion curve for Ar is the expected and usually observed behavior for γ. Now using the fitted curve for γ_{Ar} to calibrate the hyperpolarizability ratio measurements for Kr and Xe, one obtains the values given in Table III(b). Again fitting a power-series dispersion curve, one obtains the fit coefficients given in Table IV. The data and the dispersion curves for Kr and Xe are plotted in Figs. 3(c) and 3(d).

The experimental values of $\langle\gamma_{H_2}\rangle$ and $\langle\gamma_{N_2}\rangle$ are computed from the experimental ratios, using the fitted *ab initio* γ_{He} curve as before, and the results are given in Table III(a). However, determining the dispersion curves for these molecules is more complicated than for the atoms. The power series of Eq. (8) adequately describes only the electronic contribution $\langle\gamma^e\rangle$ and not the vibrational and rotational contributions $\langle\gamma^{vR}\rangle$. For ESHG, the vibrational and rotational contributions to $\langle\gamma\rangle_{zzzz}$, due to virtual transitions $0J\rightarrow v'J'$ in a homonuclear diatomic molecule in the ground vibronic state, are given by[36,37]

TABLE IV. Coefficients of the weighted least-squares fit of the function $\langle\gamma\rangle=\gamma_0[1+A\nu_L^2+B\nu_L^4]$ to the $\langle\gamma\rangle$ data in Table III. For the diatomic molecules in Table III(a), the fit was made to the experimental values of $\langle\gamma^e\rangle$. For CH_4, the $\lambda=1319$ nm point was excluded from the fit.

Gas	γ_0 (10^{-63} C^{4}m^{4}J^{-3})	A (10^{-10} cm^2)	B (10^{-20} cm^4)
Ne	7.435	−1.924	6.901
Ar	72.75	1.066	2.033
Kr	162.1	1.389	3.465
Xe	429.5	1.499	8.048
H_2	42.80	1.200	2.254
D_2	41.71	1.184	2.104
N_2	57.20	1.003	1.852
O_2	60.03	1.112	4.603
CO_2	71.50	1.252	2.405
CF_4	61.43	1.145	0.498
SF_6	89.10	0.500	2.124
CH_4	161.5	1.532	4.334
C_2H_6	292.4	2.410	3.710
C_3H_8	489.5	2.132	6.667
n-C_4H_{10}	635.9	1.573	9.730
C_4H_6	924	6.81	

$$\langle\gamma^v\rangle=\sum_{v\neq 0}\sum_J\left[\frac{4}{15}\frac{\Delta\alpha^2_{0J,vJ+2}}{\hbar\Omega_{0J,vJ+2}}\frac{(J+1)(J+2)}{(2J+1)(2J+3)}\rho(J)F(\Omega_{0J,vJ+2};\omega)\right.$$
$$+\frac{4}{15}\frac{\Delta\alpha^2_{0J+2,vJ}}{\hbar\Omega_{0J+2,vJ}}\frac{(J+1)(J+2)}{(2J+3)(2J+5)}\rho(J+2)F(\Omega_{0J+2,vJ};\omega)$$
$$\left.+\frac{8}{45}\frac{\Delta\alpha^2_{0J,vJ}}{\hbar\Omega_{0J,vJ}}\frac{J(J+1)}{(2J-1)(2J+3)}\rho(J)F(\Omega_{0J,vJ};\omega)+2\frac{\bar{\alpha}^2_{0J,vJ}}{\hbar\Omega_{0J,vJ}}\rho(J)F(\Omega_{0J,vJ};\omega)\right] \quad (9)$$

and[37,38]

$$\langle\gamma^R\rangle=\sum_J\frac{4}{15}\frac{\Delta\alpha^2_{0J,0J+2}}{\hbar\Omega_{0J,0J+2}}\frac{(J+1)(J+2)}{(2J+1)(2J+3)}$$
$$\times\left[\rho(J)-\frac{2J+1}{2J+5}\rho(J+2)\right]F(\Omega_{0J,0J+2};\omega)\ , \quad (10)$$

where

$$F(\Omega;\omega)=[1-(2\omega/\Omega)^2]^{-1}+2[1-(\omega/\Omega)^2]^{-1}\ , \quad (11)$$

$\bar{\alpha}$ and $\Delta\alpha$ are the mean and anisotropy of the Raman transition polarizability, $\rho(J)$ is the normalized rotational distribution function, and the rovibrational energy levels are given in terms of the usual spectroscopic constants[39] by

$$E(v,J)/\hbar=\omega_e(v+\tfrac{1}{2})-\omega_e x_e(v+\tfrac{1}{2})^2$$
$$+B_v J(J+1)-D_v[J(J+1)]^2\ .$$

Equations (9)–(11) are derived by neglecting the dispersion of $\bar{\alpha}$ and $\Delta\alpha$, and are valid away from exact resonance. These expressions are tedious to apply, and when the rotational transition energies are small compared to kT, Eqs. (9) and (10) may be replaced by a simpler ap-

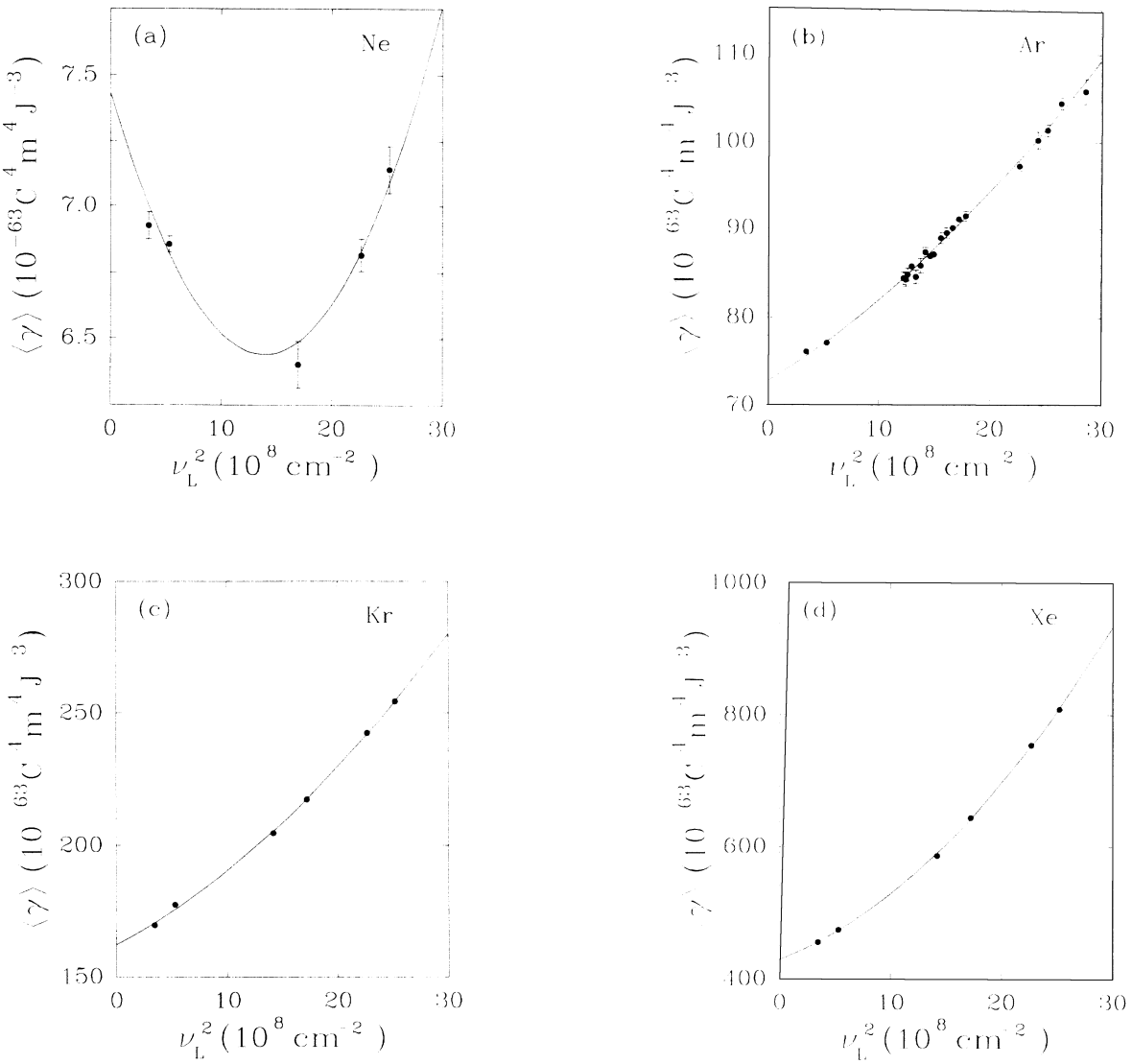

FIG. 3. Dispersion curves are shown for γ_{zzzz} as a function of ν_L^2, for the atoms Ne, Ar, Kr, and Xe [(a)–(d)]. The function $\gamma=\gamma_0(1+A\nu_L^2+B\nu_L^4)$ has been fit to the data points from Tables III(a) and III(b) (measured by ESHG over the near-infrared and visible), with the fit coefficients given in Table IV. The smooth curves show the fitted functions. The error bars for some of the data points are smaller than the plotted symbols. All frequencies involved are far below the lowest resonance frequency of any of these atoms. As expected, the dispersion increases for the sequence Ar, Kr, Xe. The negative dispersion for γ_{Ne} is anomalous.

proximate expression obtained by summing over J:

$$\langle\gamma^{vR}\rangle\approx\sum_{v\neq0}\frac{2}{\hbar\Omega_{0,v}}(\bar{\alpha}^2+\tfrac{4}{45}\Delta\alpha^2)_{0,v}F(\Omega_{0,v};\omega)+\frac{\Delta\alpha_{0,0}^2}{15kT}F(\Omega_{\mathrm{rms}};\omega)\ , \tag{12}$$

where

$$\Omega_{\mathrm{rms}}=4B_0/(\hbar B_0/kT)^{1/2} \tag{13}$$

is the effective rotational transition frequency given in terms of the ground-state rotational constant B_0. Furthermore, if the optical frequencies are much larger than the rovibrational frequencies, $\omega\gg\Omega$, one may approximate

$$F(\Omega;\omega)\approx-\tfrac{9}{4}(\Omega/\omega)^2-\tfrac{33}{16}(\Omega/\omega)^4\ . \tag{14}$$

Combining Eqs. (12)–(14) allows one to write

$$\langle\gamma^{vR}\rangle\approx G\omega^{-2}+H\omega^{-4}\ , \tag{15}$$

where G and H are weakly temperature-dependent coefficients which may be evaluated from the Raman matrix elements and transition frequencies of a homonuclear diatomic molecule. The spectroscopic constants for H_2, D_2, N_2, and O_2,[5,39–43] given in Table V, were used to calculate the coefficients G and H at $T=295$ K, also given in Table V.

For H_2 and D_2 the vibrational and rotational transition frequencies are high enough to cast doubt on the validity of the assumptions leading to Eq. (15). Therefore, $\langle\gamma^{vR}\rangle$

TABLE V. Raman transition frequencies and polarizabilities for fundamental and overtone vibrational transitions and rotational transitions. These data are used to calculate the coefficients G and H in the approximate expression $\langle\gamma^{vR}\rangle = G\nu^{-2} + H\nu^{-4}$, at $T = 295$ K. For H_2 and D_2 the values of Ω_{rms} from Eq. (13) have been slightly adjusted to improve the estimate of $\langle\gamma^R\rangle$.

	B_0	$\nu_{0,v}$ (cm^{-1})		$\Delta\alpha_{0,0}$	$(\bar{\alpha}^2 + \frac{4}{45}\Delta\alpha^2)^{1/2}_{0,v}$ (10^{-42} C^2 m^2 J^{-1})		G	H
Gas		$v=1$	$v=2$		$v=1$	$v=2$	(10^{-55} C^4 m^4 J^{-3} cm^{-2})	(10^{-48} C^4 m^4 J^{-3} cm^{-4})
H_2[a]	59.3	4156	8075	33.8	12.58	1.10	−1.591	−2.492
D_2[b]	29.9	2988	5856	32.7	10.48	0.75	−0.788	−0.632
N_2[c]	1.99	2330	4631	77	6.25	0.24	−0.221	−0.104
O_2[c]	1.44	1556	3089	122	6.15	0.12	−0.159	−0.030

[a] From Refs. 5 and 39–43 for $J = 1$.
[b] From Refs. 5 and 39–43 for $J = 2$.
[c] From Refs. 5, 39, 42, and 43.

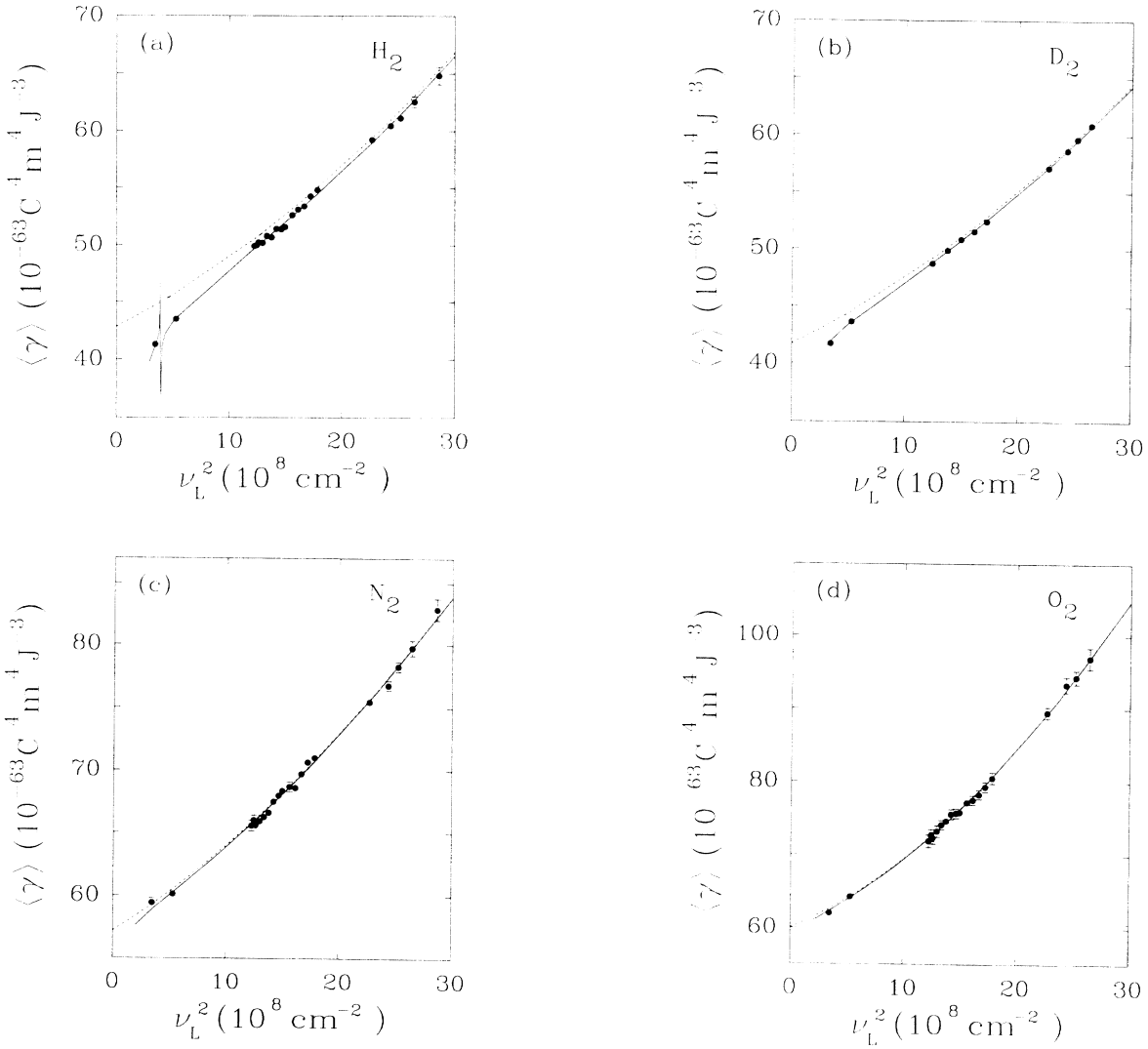

FIG. 4. Dispersion curves are shown for $\langle\gamma\rangle_{zzzz}$ as a function of ν_L^2, for the homonuclear diatomic molecules H_2, D_2, N_2, and O_2 [(a)–(d)]. Experimental data for $\langle\gamma\rangle$ are from Table III(a). The dashed lines show the least-squares fits to $\langle\gamma^e\rangle$, with coefficients given in Table IV. The solid lines are $\langle\gamma\rangle = \langle\gamma^e\rangle + \langle\gamma^{vR}\rangle$, where $\langle\gamma^{vR}\rangle$ is calculated as discussed in the text. The error bars for some of the data points are smaller than the plotted symbols. The size of $\langle\gamma^{vR}\rangle$ at optical frequencies decreases in the sequence H_2, D_2, N_2, O_2. For H_2, there are significant contributions to $\langle\gamma^{vR}\rangle$ at $\lambda = 1319$ nm due to an overtone vibrational Raman band; the closely spaced $\langle\gamma^v\rangle$ resonances near 8075 cm^{-1} actually have amplitudes $\gg\langle\gamma^e\rangle$. For all these molecules, $\langle\gamma^{vR}\rangle$ will show vibrational and rotational resonances in the infrared, and in the static limit $\langle\gamma^{vR}\rangle \geq \langle\gamma^e\rangle$.

has been evaluated for H_2 and D_2 directly from Eqs. (9)–(11), using the static polarizability matrix elements calculated by Hunt, Poll, and Wolniewicz,[40] except in the case of the vibrational overtone transitions. For the overtones, the matrix elements are the static limits of the dynamic results from the more accurate calculation of Schwartz and Le Roy.[41] The static rather than the optical polarizability matrix elements are used since $\langle \gamma^{\nu R} \rangle$ at low frequencies most critically affects the extrapolation of $\langle \gamma^{e} \rangle$ to the static limit. The values of $\langle \gamma^{\nu R}_{H_2} \rangle$ and $\langle \gamma^{\nu R}_{D_2} \rangle$ at $T=295$ K determined by these calculations are given in Table III(a). When the results of Eq. (15) for H_2 and D_2 are compared with the results of Eqs. (9)–(11), one sees that Eq. (15) is significantly in error for the near-infrared wavelengths, but it is in fact accurate to better than 0.01×10^{-63} $C^4m^4J^{-3}$ for all visible wavelengths. For N_2 and O_2 the $\langle \gamma^{\nu R} \rangle$ contribution is much smaller (0.1% of $\langle \gamma \rangle$ in the visible), so Eq. (15) is more than adequately accurate for N_2 and O_2 at all wavelengths of present interest.

The analysis of the H_2 and D_2 data proceeds as follows. By simple subtraction of the results in Table III(a), one obtains the experimental values of $\langle \gamma^{e}_{H_2} \rangle = \langle \gamma_{H_2} \rangle - \langle \gamma^{\nu R}_{H_2} \rangle$, which are then fit with a power series dispersion curve, just as in the atomic case (coefficients in Table IV). The sum of the fitted $\langle \gamma^{e}_{H_2} \rangle$ curve and calculated $\langle \gamma^{\nu R}_{H_2} \rangle$ values is the desired dispersion curve for $\langle \gamma_{H_2} \rangle$. This curve is plotted in Fig. 4(a) along with the $\langle \gamma_{H_2} \rangle$ data from which it was obtained. The dispersion curve for $\langle \gamma_{H_2} \rangle$ also serves to calibrate the $\langle \gamma_{D_2} \rangle$ results given

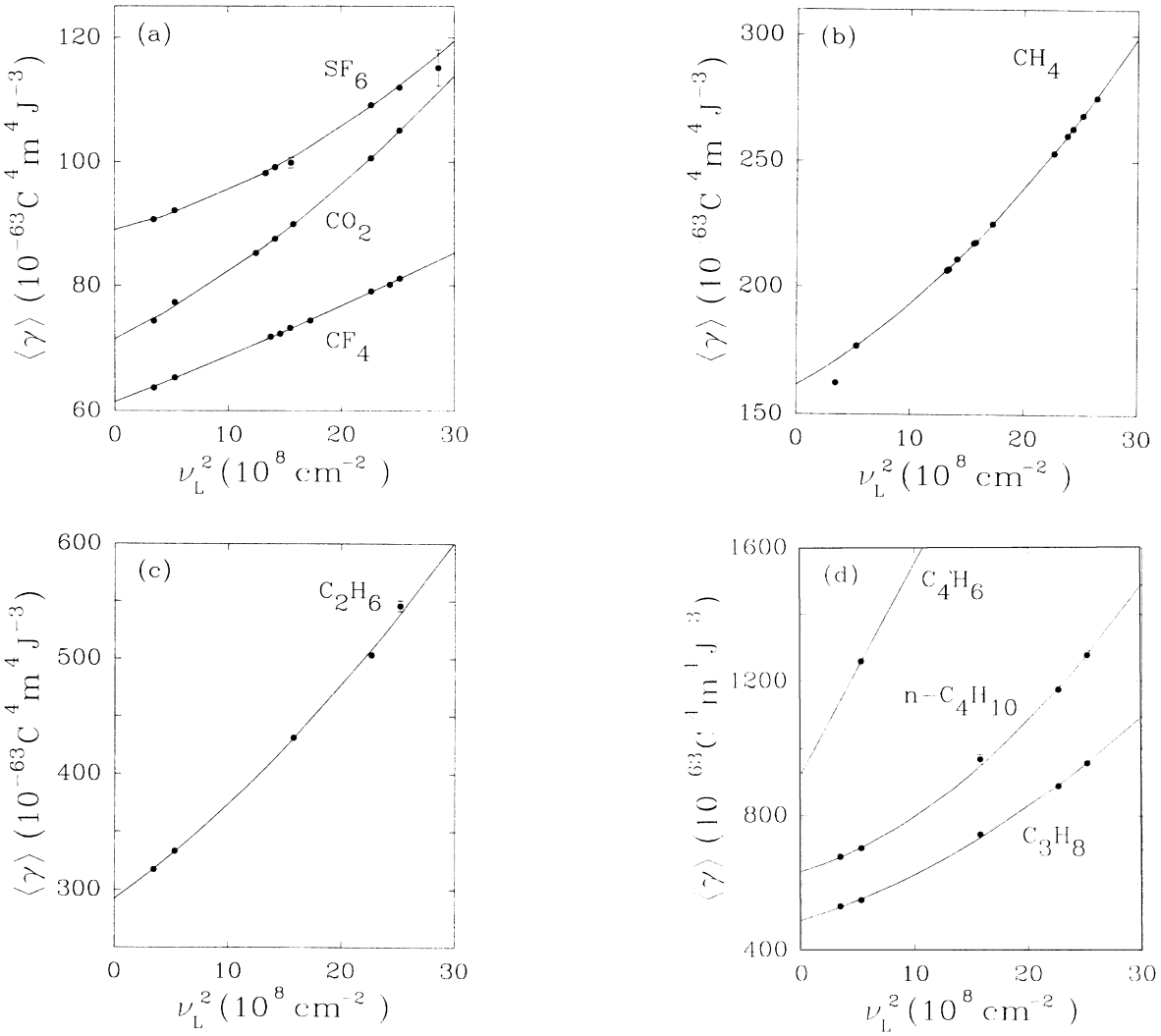

FIG. 5. Dispersion curves are shown for $\langle \gamma \rangle_{zzzz}$ as a function of ν_L^2, for the polyatomic molecules (a) CO_2, CF_4, and SF_6; (b) CH_4; (c) C_2H_6; and (d) C_3H_8, n-C_4H_{10}, and C_4H_6. Power law dispersion curves have been fit without separately accounting for $\langle \gamma^{\nu R} \rangle$ [data in Tables III(b) and III(c); fit coefficients in Table IV]. These curves will not adequately represent $\langle \gamma \rangle$ near $\nu_L^2=0$. The error bars for some of the data points are smaller than the plotted symbols. Except for $\langle \gamma_{CH_4} \rangle$, these fits adequately represent the data. For CH_4, the large discrepancy for the $\lambda=1319$ nm point (excluded from the fit) indicates that $\langle \gamma^{\nu R} \rangle$ may significantly alter the shape of the dispersion curve even at visible wavelengths.

in Table III(a). Proceeding as for H_2, one obtains and fits $\langle \gamma^e_{D_2} \rangle$, yielding the coefficients given in Table IV. The dispersion curve for $\langle \gamma_{D_2} \rangle$ is again the sum of the fitted $\langle \gamma^e_{D_2} \rangle$ curve and the calculated $\langle \gamma^{vR}_{D_2} \rangle$. This dispersion curve for $\langle \gamma_{D_2} \rangle$ is compared with the data in Fig. 4(b). The analysis of the N_2 and O_2 data is exactly the same as for H_2 and D_2, except that Eq. (15), with the coefficients from Table V, is used to calculate $\langle \gamma^{vR} \rangle$. Figures 4(c) and 4(d) show the dispersion curves and the data for $\langle \gamma_{N_2} \rangle$ and $\langle \gamma_{O_2} \rangle$.

The dispersion curve for $\langle \gamma_{N_2} \rangle$ finally serves to calibrate the ratio data for the remaining molecules, with the resulting $\langle \gamma \rangle$ values given in Tables III(b) and III(c). Ideally, the electronic and vibrational contributions to $\langle \gamma \rangle$ should be separately dealt with in the determination of the $\langle \gamma \rangle$ dispersion curves for the polyatomic molecules. Expressions for the vibrational contributions for tetrahedral and octahedral molecules have been derived, but these expressions are very complicated, as well as requiring presently unobtainable molecular property data for their accurate evaluation.[44] For a number of molecules in this study the appropriate expressions for $\langle \gamma^{vR} \rangle$ have not been derived. However, in contrast to the strong ω^{-2} frequency dependence of $\langle \gamma^{vR} \rangle$ for the diatomic molecules, it appears that $\langle \gamma^{vR} \rangle$ is nearly constant at optical frequencies for polyatomic molecules such as CF_4 and SF_6 (for ESHG).[23,44] Furthermore, it is estimated that $\langle \gamma^{vR} \rangle$ is only about 1% of $\langle \gamma \rangle$ for CH_4 (for ESHG),[32,45] and the same may be true for the other hydrocarbon molecules studied. If this is the case, a power series dispersion curve should be an adequate representation of $\langle \gamma \rangle$. Accordingly, Eq. (8) has been used to fit the remaining data, with the fit coefficients given in Table IV. The fitted curves and the $\langle \gamma \rangle$ data for the polyatomic molecules are plotted in Figs. 5(a)–5(d).

DISCUSSION

The fitted curves adequately represent the data, with one significant exception for CH_4. Though the older data for Ar, H_2, and N_2 appears somewhat ragged, the absolute accuracy of the $\langle \gamma \rangle$ dispersion curves for Ar, H_2, and N_2 (calibrated directly against He) is expected to be about 0.2% over the fitted range. The extrapolation to the static limit of $\langle \gamma^e \rangle$ for the atoms and diatomic molecules should be accurate to about 0.5%, but relies heavily on the accuracy of the infrared data (the $\lambda = 1064$ nm point in particular), and in the case of the diatomic molecules, also on the accuracy of the $\langle \gamma^{vR} \rangle$ calculation. For Ne, the nonmonotonic dispersion curve increases the uncertainty of the estimated static value of γ to about 2%.

However, there are several systematic defects which should be considered. First, a recent calculation indicates that the effect of pair interactions between He atoms in a gas, at the highest densities employed in these experiments, may increase $\chi^{(3)}$ for the gas by 1% compared to the value calculated for a gas of noninteracting He atoms.[46] The effect is expected to be half as large for Ne.[46] If this calculation is correct, all the experimental estimates of $\langle \gamma \rangle$ given here should be adjusted upward by about 1%, except γ_{Ne} which should only increase half as much. Once the interaction contributions are accurately known, the measured $\langle \gamma \rangle$ may easily be corrected for the interaction effects.

Second, for the dipolar species C_3H_8, n-C_4H_{10}, and C_4H_6, the measured $\langle \gamma \rangle$ is actually contaminated by a temperature-dependent $\mu^{(0)}\beta/3kT$ term. This contribution had been considered previously for C_3H_8 and n-C_4H_{10} and was judged to be small ($<3\%$);[33] measurements of the temperature dependence of $\chi^{(3)}$ for C_4H_6 indicate a $7\pm6\%$ contribution at room temperature.[34] By leaving the temperature dependence of $\chi^{(3)}$ unaccounted for, we may have incurred errors of several percent in $\langle \gamma \rangle$ for these molecules. Accurate measurements of the expected weak temperature dependence of $\chi^{(3)}$ for these molecules would allow one to eliminate this defect.

Third, there is the difficulty of adequately assessing $\langle \gamma^{vR} \rangle$ for the polyatomic molecules, which makes the extrapolation to the static limit problematic. For CH_4, the $\lambda = 1319$ nm point misses the dispersion curve by 12 standard deviations [Fig. 5(b)], which is a clear indication that the curve should actually bend down at low frequencies as in the case of H_2 [Fig. 4(a)]. There are two strong fundamental Raman bands[47] near 3000 cm^{-1} for CH_4 which could make $\langle \gamma^{vR} \rangle$ for CH_4 larger than that for H_2 (the overtone bands near 6000 cm^{-1} probably do not play a major role),[48] and significantly alter the shape of the dispersion curve even at visible wavelengths. More information is needed for a conclusive interpretation, especially since no discrepancy at $\lambda = 1319$ nm is observed for the other alkanes [Figs. 5(c) and 5(d)]. A possible way to attack the problem of determining $\langle \gamma^{vR} \rangle$ is by combining theoretical calculations with experimental measurements of the frequency dependence of $\langle \gamma \rangle$ for both the dc Kerr effect and ESHG.

Until the above-mentioned defects are corrected or resolved, the effective accuracy of our results is only about 1%, even for the atoms and diatomic molecules. Since $\langle \gamma^{vR} \rangle$ cannot at present be adequately assessed for the polyatomic molecules, we are unable to accurately determine $\langle \gamma^e \rangle$ or its static limit for these molecules. Despite these shortcomings, the results of this work have several interesting features and allow some conclusions to be drawn. First of all, this work provides reasonably accurate $\langle \gamma \rangle$ dispersion curves for a large enough set of atoms and molecules to allow one to pick out the exceptional cases. The negative A dispersion coefficient for Ne clearly marks Ne as an exception. Also, the dispersion coefficients for CF_4 and SF_6 indicate that the $\langle \gamma \rangle$ dispersion curve for CF_4 is unusually straight, while the curve for SF_6 has an unusually small initial slope. These may be the signatures of unusually large vibrational contributions to $\langle \gamma \rangle$.

The experimental estimates of the static limits of $\langle \gamma^e \rangle$ for Ne, Ar, H_2, and D_2 allow one to assess the results of the presently most accurate *ab initio* calculations for Ne,[49] Ar,[50] H_2, and D_2.[9] All these calculations include electron correlations and employ large basis sets. The calculations for Ne and Ar include triple excitations in a

coupled-cluster correlation treatment, while for H_2 and D_2 the interelectronic coordinate explicitly appears in the wave function. For H_2 and D_2, $\langle\gamma\rangle$ at optical frequencies has also been calculated,[9] but for Ne and Ar only the static results were obtained. Converting the values of γ_0 given in Table IV for Ne, Ar, and H_2 to atomic units (conversion factor with $\mu=m_e$ is $6.235\,377\times10^{-65}$ $C^4m^4J^{-3}$), one has the experimental estimates $\langle\gamma^e\rangle_{\omega=0}=119\pm2$ a.u., 1167 ± 6 a.u., and 686 ± 4 a.u. for Ne, Ar, and H_2, respectively. The stated uncertainties do not include possible systematic errors in the calibration due to the effect of He pair interactions. The corresponding *ab initio* results are $\langle\gamma^e\rangle_{\omega=0}=119\pm4$ a.u., 1220 ± 30 a.u., and 671 ± 6 a.u. The differences between the *ab initio* and experimental results for $\langle\gamma^e\rangle_{\omega=0}$ are 0.0%, +4.5%, and −2.2% for Ne, Ar, and H_2, respectively. The anticipated corrections to the experimental results, due to the effects of pair interactions for He and Ne at high densities, would change the differences between the *ab initio* results and the experimental estimates to −0.5%, +3.2%, and −3.2%. The *ab initio* results for Ne seem to have converged, and the result for Ar seems quite good considering the large size of the Ar atom. Though these calculations are difficult, it seems that the *ab initio* techniques presently being used to calculate γ for atoms will be adequate even for heavy atoms. The situation seems less satisfactory for molecules, since even a very careful calculation for H_2 apparently achieves only 2% accuracy.

The experimental results for H_2 may be checked by comparing them with the measurements for D_2. The experimental and *ab initio* results for $\langle\gamma^e_{H_2}\rangle/\langle\gamma^e_{D_2}\rangle$ in the static limit are 1.026 and 1.029,[9] respectively. The agreement between experiment and theory for the ratio $\langle\gamma^e_{H_2}\rangle/\langle\gamma^e_{D_2}\rangle$ is an indication that the calculation of $\langle\gamma^{vR}\rangle$ is adequate for H_2 and D_2, and that the experiment extrapolation to the static limit is accurate. As a further check, the experimental and *ab initio* values of $\langle\gamma^e_{H_2}\rangle$ at $\lambda=488.0$ nm are 992 and 969 a.u.,[9] respectively; the −2.4% discrepancy at optical frequencies is consistent with the −2.2% static discrepancy, and this again supports the accuracy of our experimental extrapolation to the static limit for H_2. Note that this last result is insensitive to small errors in $\langle\gamma^{vR}_{H_2}\rangle$, which only contributes 0.6% of $\langle\gamma_{H_2}\rangle$ at $\lambda=488.0$ nm, and that the anticipated correction for He pair interactions will make the disagreement even worse. The disagreement between theory and experiment for H_2 is larger than previously estimated, but the previous comparison[9] was based on incorrect values for γ_{He}.[25] It is possible that the disagreement is due to the effect of pair interactions on γ for H_2. If the pair-interaction effects are much stronger for H_2 than for He, then they could be significant at even the relatively low H_2 sample densities employed in these measurements.

The *ab initio* calculation of $\langle\gamma\rangle$ for the H_2 molecule is much more difficult than for an atom, since there are seven independent tensor components of γ to compute as functions of the internuclear coordinate. Nevertheless, even a 2% discrepancy is surprising, considering that a basis of up to 249 explicitly electron-correlated functions has been used to describe the wave function of this two-electron system. For He, a basis set half this size is thought to give 0.02% accuracy. Calculations for molecules much larger than H_2 usually employ a smaller basis set of uncorrelated functions and fix the nuclei at their equilibrium positions.[7,51–54] Both static[51,53] and dynamic[7,52,54] calculations of γ have been performed, with[7,53,54] and without[51,52] inclusion of electron correlation. Hartree-Fock calculations for N_2,[51] CH_4, and CF_4 (Ref. 52) give the static values of $\langle\gamma\rangle=700$, 452, 143 a.u., respectively, to be compared with 917, 2590, and 985 a.u. from the static limit of our experimental results. The agreement is rather poor, possibly due to the neglect of electron correlation. But even when electron correlation is included, for example in calculations for several conjugated molecules,[7,54] the accuracy of the calculated results remains an open question.

ACKNOWLEDGMENTS

This work was supported in part by a grant from the Natural Sciences and Engineering Research Council of Canada.

[1]Y. R. Shen, *Principles of Nonlinear Optics* (Wiley, New York, 1984).
[2]M. D. Levenson, *Introduction to Nonlinear Laser Spectroscopy* (Academic, New York, 1982).
[3]N. B. Delone and V. P. Krainov, *Fundamentals of Nonlinear Optics of Atomic Gases* (Wiley, New York, 1988).
[4]D. C. Hanna, M. A. Yuratich, and D. Cotter, *Nonlinear Optics of Free Atoms and Molecules* (Springer, Berlin, 1979).
[5]M. P. Bogaard and B. J. Orr, in *International Review of Science, Physical, Chemistry, Molecular Structure and Properties*, edited by A. D. Buckingham (Butterworths, London, 1975), Ser. 2, Vol. 2, p. 149.
[6]G. T. Boyd, J. Opt. Soc. Am. B **6**, 685 (1989).
[7]J. W. Wu, J. R. Heflin, R. A. Norwood, K. Y. Wong, O. Zamani-Khamiri, A. F. Garito, P. Kalyanaraman, and J. Sounik, J. Opt. Soc. Am. B **6**, 707 (1989).
[8]D. M. Bishop and B. Lam, Mol. Phys. **62**, 721 (1987).
[9]D. M. Bishop and B. Lam, J. Chem. Phys. **89**, 1571 (1988); D. M. Bishop, J. Pipin, and M. Rérat, J. Chem. Phys. **92**, 1902 (1990).
[10]D. P. Shelton and A. D. Buckingham, Phys. Rev. A **25**, 2787 (1982).
[11]V. Mizrahi and D. P. Shelton, Phys. Rev. A **31**, 3145 (1985).
[12]D. P. Shelton, Rev. Sci. Instrum. **56**, 1474 (1985).
[13]V. Mizrahi and D. P. Shelton, Phys. Rev. A **32**, 3454 (1985).
[14]A. Yariv, *Introduction to Optical Electronics* (Holt, Rinehart and Winston, New York, 1976).
[15]D. P. Shelton and V. Mizrahi, Phys. Rev. A **33**, 72 (1986).
[16]J. Marling, IEEE J. Quant. Electron. **QE-14**, 56 (1978).
[17]J. H. Dymond and E. B. Smith, *The Virial Coefficients of Pure Gases and Mixtures* (Clarendon, Oxford, 1980).
[18]Landolt-Börnstein, *Zahlenwerte und Funktionen* (Springer,

Berlin, 1962), Band II, Teil 8.
[19]P. J. Leonard, At. Data Nucl. Data Tables **14**, 21 (1974).
[20]A. D. Buckingham and H. Sutter, J. Chem. Phys. **64**, 364 (1976).
[21]D. A. Dunmur, D. C. Hunt, and N. E. Jessup, Mol. Phys. **37**, 713 (1979).
[22]D. P. Shelton, J. Chem. Phys. **85**, 4234 (1986).
[23]Z. Lu and D. P. Shelton, J. Chem. Phys. **87**, 1967 (1987).
[24]D. M. Bishop and J. Pipin, J. Chem. Phys. **91**, 3549 (1989).
[25]D. M. Bishop and B. Lam, Phys. Rev. A **37**, 464 (1988).
[26]D. M. Bishop, Chem. Phys. Lett. **153**, 441 (1988); J. Chem. Phys. **90**, 3192 (1989).
[27]E. R. Cohen and B. N. Taylor, Rev. Mod. Phys. **59**, 1121 (1987).
[28]V. Mizrahi and D. P. Shelton, Phys. Rev. Lett. **55**, 696 (1985).
[29]D. P. Shelton, J. Chem. Phys. **84**, 404 (1986).
[30]D. P. Shelton, Phys. Rev. Lett. **62**, 2660 (1989); D. P. Shelton and Z. Lu, Phys. Rev. A **37**, 3813 (1988).
[31]D. P. Shelton and V. Mizrahi, Chem. Phys. Lett. **120**, 318 (1985).
[32]D. P. Shelton, Phys. Rev. A **34**, 304 (1986).
[33]R. E. Cameron and D. P. Shelton, Chem. Phys. Lett. **133**, 520 (1987).
[34]J. F. Ward and D. S. Elliott, J. Chem. Phys. **69**, 5438 (1978).
[35]R. S. Finn and J. F. Ward, Phys. Rev. Lett. **26**, 285 (1971); J. F. Ward and I. J. Bigio, Phys. Rev. A **11**, 60 (1975); J. F. Ward and C. K. Miller, *ibid.* **19**, 826 (1979).
[36]D. P. Shelton, Mol. Phys. **60**, 65 (1987).
[37]D. M. Bishop, Rev. Mod. Phys. **62**, 343 (1990).
[38]D. P. Shelton, Phys. Rev. A **36**, 3461 (1987); D. M. Bishop and D. P. Shelton, *ibid.* **38**, 1656 (1988).
[39]S. Brodersen, in *Topics in Current Physics, Raman Spectroscopy of Gases and Liquids,* edited by A. Weber (Springer, Berlin, 1979), Vol. 11, p. 7; A. Weber, *ibid.*, p. 71; I. N. Levine, *Quantum Chemistry, Vol. II, Molecular Spectroscopy* (Allyn and Bacon, New York, 1970).
[40]J. L. Hunt, J. D. Poll, and L. Wolniewicz, Can. J. Phys. **62**, 1719 (1984).
[41]C. Schwartz and R. J. Le Roy, J. Mol. Spectrosc. **121**, 420 (1987).
[42]W. Knippers, K. Van Helvoort, and S. Stolte, Chem. Phys. Lett. **121**, 279 (1985).
[43]H. W. Schrötter and H. W. Klöckner, in *Topics in Current Physics, Raman Spectroscopy of Gases and Liquids* (Ref. 39), Vol. 11, p. 123.
[44]D. P. Shelton and L. Ulivi, J. Chem. Phys. **89**, 149 (1988).
[45]D. S. Elliott and J. F. Ward, Mol. Phys. **51**, 45 (1984).
[46]M. G. Papadopoulos and J. Waite, Chem. Phys. Lett. **135**, 361 (1987).
[47]W. F. Murphy, W. Holzer, and H. J. Bernstein, Appl. Spectrosc. **23**, 211 (1969).
[48]L. Halonen and M. S. Child, Mol. Phys. **46**, 239 (1982).
[49]P. R. Taylor, T. J. Lee, J. E. Rice, and J. Almlöf, Chem. Phys. Lett. **163**, 282 (1989).
[50]P. R. Taylor (unpublished).
[51]C. J. Jameson and P. W. Fowler, J. Chem. Phys. **85**, 3432 (1986).
[52]H. Sekino and R. J. Bartlett, J. Chem. Phys. **85**, 976 (1986).
[53]G. Maroulis and A. J. Thakkar, J. Chem. Phys. **90**, 366 (1988).
[54]B. M. Pierce, J. Chem. Phys. **91**, 791 (1989).